Variation of the Corrosion Behavior Prior to Crack Initiation of E690 Steel Fatigued in Simulated Seawater with Various Cyclic Stress Levels

Tianliang Zhao, Zhiyong Liu, Liu Chao, Chunduo Dai, Cuiwei Du, and Xiaogang Li

The electrochemical process and corrosion behavior prior to crack initiation of E690 steel fatigued in simulated seawater are investigated under different cyclic stress levels by methods of electrochemical impedance spectroscopy, cyclic current response, electrochemical noise and morphology observation. The results show that the electrochemical behavior changes with the peak stress of cyclic loading and the corrosion behavior transforms as the peak stress increases over the proof strength. The charge transfer resistance (R_{ct}) decreases with elevated peak stress. Continuous decreasing R_{ct} with cycling number under peak stress of 1.02 $\sigma_{p0.2}$ indicates that continuous fresh metal induced by work-softening is exposed to the seawater, which is also proved by cyclic current response induced by cyclic stress and contact angle test. As a result, the corrosion type of E690 steel changes from general corrosion to pitting corrosion with the peak stress close to and above the proof strength. That induces the corrosion fatigue crack initiation mechanism to change correspondingly.

1. Introduction

It is extensively realized that corrosion can dramatically shorten fatigue crack initiation life by up to 90% than that in air (Ref 1). The corrosion is mainly attributed to the synergistic effect of the corrosive medium and cyclic load, which can be theoretically explained with the well-known mechanochemical and chemomechanical effects (Ref 2, 3). However, due to different material properties, loading and environmental conditions, the synergistic effect usually behaves complicatedly, making corrosion prior to crack complex and inducing a different corrosion fatigue crack initiation (CFCI) mechanism.

Numerous studies (Ref 4-17) concluded that cyclic load had a great effect on corrosion or electrochemical behaviors of metals in media and hence exerted an effect on the crack initiation behaviors and mechanisms. Guan et al. (Ref 9) found that cyclic stress with peak value above yield strength evidently promoted occurrence of the metastable pitting and decreased the pitting potential, while those with peak values below the yield strength had barely no effect on corrosion behavior. Ebara (Ref 4) monitored the corrosion process prior to crack initiation of 12Cr stainless steel by the electrochemical noise method and

found that cyclic stress level had a positive influence on the formation of stable pits. Pyle et al. (Ref 6) revealed that the effects of cyclic loading on the stable or metastable pitting prior to crack initiation were actually related to polarization potentials: the maximum transient current was observed when the polarization potential was at the active/passive transition zone. Moreover, the literature (Ref 7, 8, 10) also reported that cyclic load would result in a non-faradic current response which could provide useful information about the mechanochemical and chemomechanical effects, the corrosion fatigue damage or the crack initiation detection. Those works mentioned above provided a further understanding about CFCI from the perspective of electrochemistry or corrosion. Nevertheless, they could not fit the CFCI of carbon steels well due to the quite different surface properties of the stainless steels they focused on.

Certain researchers (Ref 5, 11, 12, 18-22) tried to characterize the electrochemical behaviors of carbon steel before crack initiation. Different from stainless steel, the CFCI mechanism of carbon steel or low-alloy steel is no longer simple slipping-film rupture–re-passivation cyclic process and may be more complex due to its inability to form a compact film on surface. The corrosion behaviors of carbon steels or low-alloy steels show relatively less sensitivity to stress. Thus, most of the previous studies failed to correlate the electrochemical behaviors or corrosion behaviors with crack initiation (Ref 16).

Herein, we use a low-carbon bainite steel, named E690 steel, as the study material. The effects of cyclic stress on the electrochemical behavior and corrosion behavior prior to CFCI are investigated in simulated seawater by electrochemical impedance spectroscopy, cyclic current response and electrochemical noise. The peak stress both under and above the proof strength is chosen for the experiments. Based on the results, the relationship between the corrosion behavior and the CFCI mechanism is discussed and concluded.

Tianliang Zhao, Zhiyong Liu, Liu Chao, Chunduo Dai, and **Cuiwei Du**, Corrosion and Protection Center, University of Science and Technology Beijing, Beijing 100083, China; and **Xiaogang Li**, Key Laboratory of Chinese Ministry of Education for Corrosion and Prevention, University of Science and Technology Beijing, Beijing 100083, China; and Ningbo Institute of Material Technology and Engineering, Chinese Academy of Sciences, Ningbo 315201, China. Contact e-mails: ustb_tlzhao@163.com and   and   and dcw@ustb.edu.cn.

2. Materials and Experiments

2.1 Materials and Medium

E690 steel is a newly developed low-carbon bainite steel for large marine stages and ships. Its chemical composition, in weight percent (wt.%), is given as follows: 0.15 C, 0.20 Si, 1.00 Mn, P 0.0058 P, 0.0014 S, 0.99 Cr, 1.45 Ni, 0.0091 Cu, 0.37 Mo, 0.03 V, 0.036 Als and balance Fe. Triplicate tensile tests show that E690 steel has 0.2% offset proof strength of 770 MPa, tensile strength of 848 MPa, elongation of 24.44 average% and reduction of area of 75.61 average%. The E690 steel used in this study is as-received and its microstructure is mainly composed of granular and lath bainite, which can be seen in our previous study (Ref 23).

The corrosion solution used in this study is simulated seawater prepared according to the ASTM standard D1141-98(2013). The pH value is modulated to 8.2 with 0.1 mol/L NaOH solution.

2.2 Electrochemical Tests During Cyclic Loading

Specimens for electrochemical tests during cyclic loading were machined into hourglass-like sheets with thickness of 2 mm and 5 mm wide in the gauge section. The loading pins were intertwined with glass fiber cloth in order to insulate the specimens from the fatigue machine (MTS, Landmark 370). Both the gauge section of the fatigue specimens and stress-free specimens were wet-ground manually with a series of emery papers from 800 to 5000 grit, then degreased with alcohol and rinsed with deionized water. The stress-free specimens were welded to a copper wire for electrical connection and then mounted in the epoxy resin with a testing window (5 mm × 5 mm) exposed. Gauge sections of the fatigue specimens were covered with silica rubber, leaving a testing window with size of 5 mm × 5 mm exposed.

Setup for electrochemical tests during cyclic loading is shown in Fig. 1. The fatigue specimen (WE$_1$), the standard calomel electrode (SCE) and the platinum foil were used as the working, the reference and the counter electrodes, respectively, in the electrochemical impedance spectroscopy (EIS) measurements. The stress-free specimen (WE$_2$), the WE$_1$ and the SCE were used as the second working, the first working and the reference electrodes, respectively, in the electrochemical noise (EN) measurements. In order to avoid the interference of the outside electromagnetic signals, the whole setup was shielded with copper wire mesh.

The electrochemical measurements were taken under different cyclic stress levels with peak stresses of 0 MPa, 0.6 $\sigma_{p0.2}$ (462 MPa), 0.8 $\sigma_{p0.2}$ (616 MPa), 0.95 $\sigma_{p0.2}$ (732 MPa) and 1.02 $\sigma_{p0.2}$ (785 MPa), respectively. The cyclic stress waveform was sinusoidal, the stress ratio was 0.1, and the loading frequency was 1 Hz. The EIS measurements were taken on a CHI-660E electrochemical working station. The EN measurements were taken on a Corrtest CST500 electrochemical noise instrument. The EN and EIS measurements with one cyclic stress level could be taken successively in one experiment. Proper intervals were set between each measurement. The EIS measurements were taken at open-circuit potential (OCP). Amplitude of the stimulus signal was 5 mV. The frequency ranged from 0.01 Hz to 100 kHz. The EN measurement included two parts: The first part was used to record the waveform of current response. Time and frequency of data collection were 10 s and 20 Hz. The second part was measured for time-domain and frequency-domain analysis of EN signals. Duration and frequency of data collection were 1024 s and 2 Hz.

3. Results

3.1 EIS Under Cyclic Loading

EIS measurements were taken on E690 steel in simulated seawater with various peak stresses during the corrosion fatigue. Figure 2 shows the Nyquist curves at different fatigue time with various peak stresses and the corresponding equivalent circuits, as well as the corresponding fitting curves. It is noted in Fig. 2(b), (c), (d) and (e) that inductance tails appear at
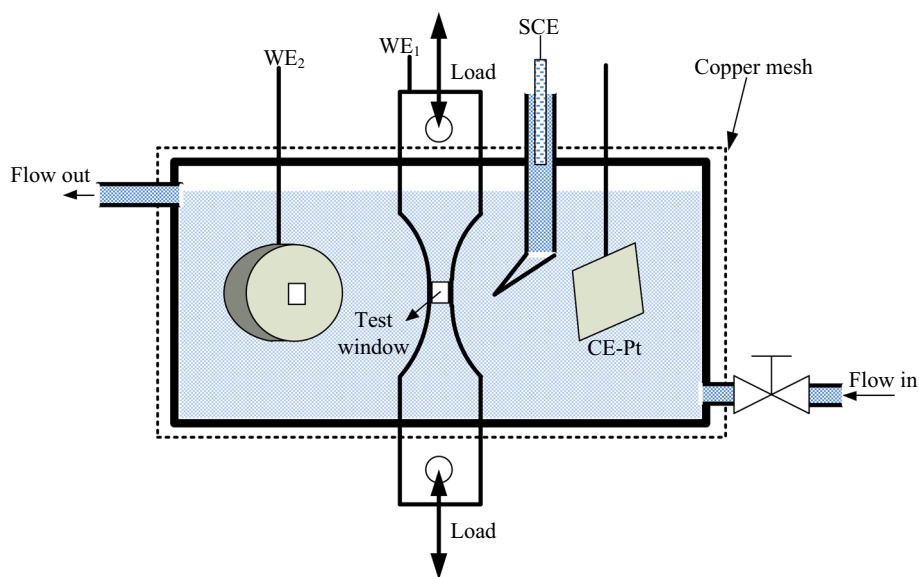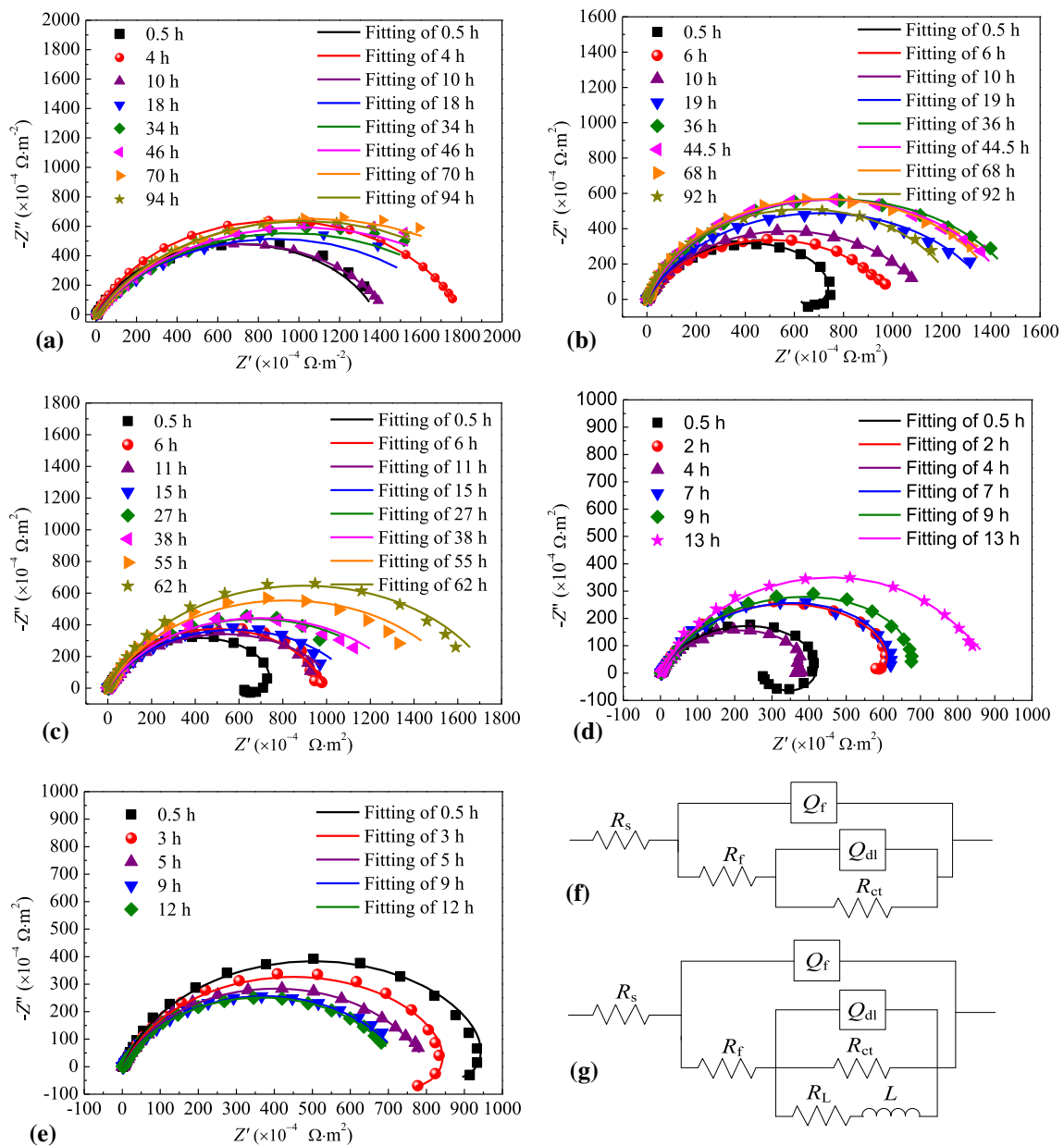

**Fig. 1** Setup for electrochemical tests during cyclic loading

Fig. 2 EIS of E690 steel fatigued in simulated seawater for different time with various peak stresses: (a) stress free, (b) 0.6 $\sigma_{p0.2}$, (c) 0.8 $\sigma_{p0.2}$, (d) 0.95 $\sigma_{p0.2}$, (e) 1.02 $\sigma_{p0.2}$, (f) the equivalent circuit for EIS without inductance, (g) the equivalent circuit for EIS with inductance

the low-frequency region of early Nyquist curves with cyclic stresses. Compared with the stress-free specimen, the surface of the specimen loaded with cyclic stress keeps moving up and down repeatedly during the measurement. The up-down movement makes matter absorb on the surface and desorb again. Repeated absorption and desorption contribute to the inductance tail on the Nyquist curve. Physical implication of the electric parameters in Fig. 2(f) and (g) is as follows: R_s is the solution resistance from the tip of Luggin capillary to the surface of specimens; Q_f is the capacitance of the surface product layer; R_f is the resistance of the surface product layer; Q_{dl} is the capacitance of the electrical double layer; R_{ct} is the charge transfer resistance; and R_L and L are the resistance and the capacitance related to the absorption process on the interface. It can be seen from Fig. 2 that the radius of the capacitive arc in the Nyquist curve increases gradually with

elapsed cycling time when the peak stress is below the proof strength, while it decreases gradually with cyclic time elapsed when the peak stress is above the proof strength (namely 1.02 $\sigma_{p0.2}$). It is also noted in Fig. 2(b) that the radius of the arc decreases from 36 to 92 h. We deem that the decrease does not represent an intrinsic change on the electrode surface. Since the product layer is porous, it would partly fall off, making the radius of the arc decrease. The radius of the arc would stabilize within a certain range until the fatigue fracture.

The Nyquist curves with and without inductance tails were fitted with the equivalent circuit in Fig. 2(f) and (g). The fitted values of R_{ct} under cyclic loading with various peak stresses are re-plotted in Fig. 3. In order to facilitate the comparison, the abscissa is normalized with cycles (N) divided by cycles to failure (N_a). Value of N/N_a actually indicates the accumulated corrosion fatigue damage. It is seen that R_{ct} increases with
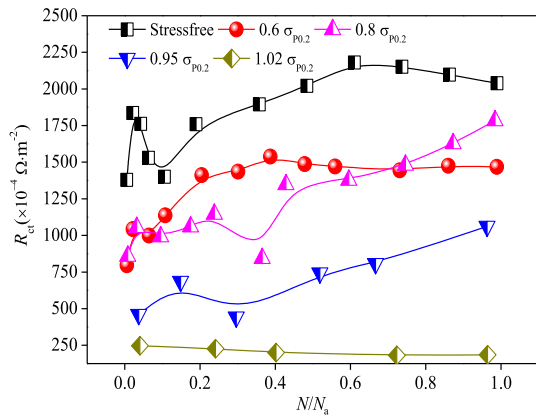
Fig. 3 Value of R_{ct} vs. N/N_a of E690 steel in simulated seawater under cyclic loading with various peak stresses
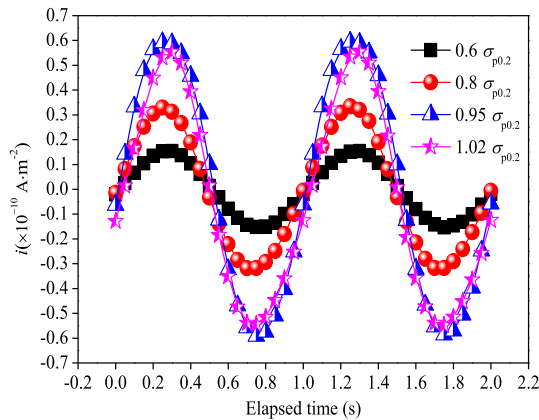
Fig. 4 Cyclic current responses induced by cyclic stresses under cyclic loading with various peak stresses: (a) 0.6 $\sigma_{p0.2}$, (b) 0.8 $\sigma_{p0.2}$, (c) 0.95 $\sigma_{p0.2}$, (d) 1.02 $\sigma_{p0.2}$
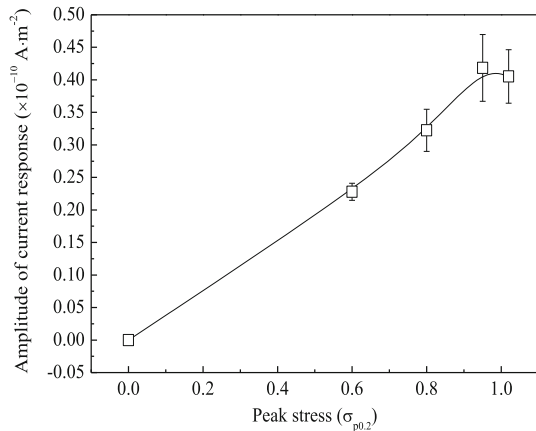
Fig. 5 Variation of the amplitude of the sinusoidal cyclic current response with peak stress

increased N/N_a when peak stress is below the proof strength, while it decreases when the peak stress is above the proof strength (1.02 $\sigma_{p0.2}$). It should be attributed to the different deformation behaviors under different peak stresses. Under cyclic loading with peak stress of 1.02 $\sigma_{p0.2}$, the specimens

suffer work-softening, making dislocations continuously slip outside the surface and expose fresh substrate to seawater. So that the electrochemical reactions are promoted and R_{ct} keeps decreasing. Moreover, it is seen that R_{ct} decreases with peak stress increased for zero to 1.02 $\sigma_{p0.2}$. It indicates that cyclic stress with peak stress even below the proof strength can still promote the electrochemical reactions.

3.2 Cyclic Current Response Under Cyclic Loading

Current response to cyclic loading was found during the EN measurements. In order to obtain the full curves, data collection frequency of 20 Hz was applied on monitoring the current response. A window of 2 s is taken from each current response. And the base currents are also removed with linear fitting. Figure 4 shows the sinusoidal current responses under cyclic loading with different peak stresses. It is seen that amplitude of the current response increases obviously with increased peak stress when peak stress is below the proof strength, while the trend fades or even tends to decrease when the peak stress is above the proof strength.

The average amplitudes of current responses under each peak stress were calculated and plotted against peak stress, as shown in Fig. 5. It is seen that the average amplitude increases linearly with increased peak stress from zero to 0.95 $\sigma_{p0.2}$ and deviates from linearity at 1.02 $\sigma_{p0.2}$. These phenomena will provide useful information about the CFCI mechanisms (Ref 8). It will be discussed further in the "Discussion" section.
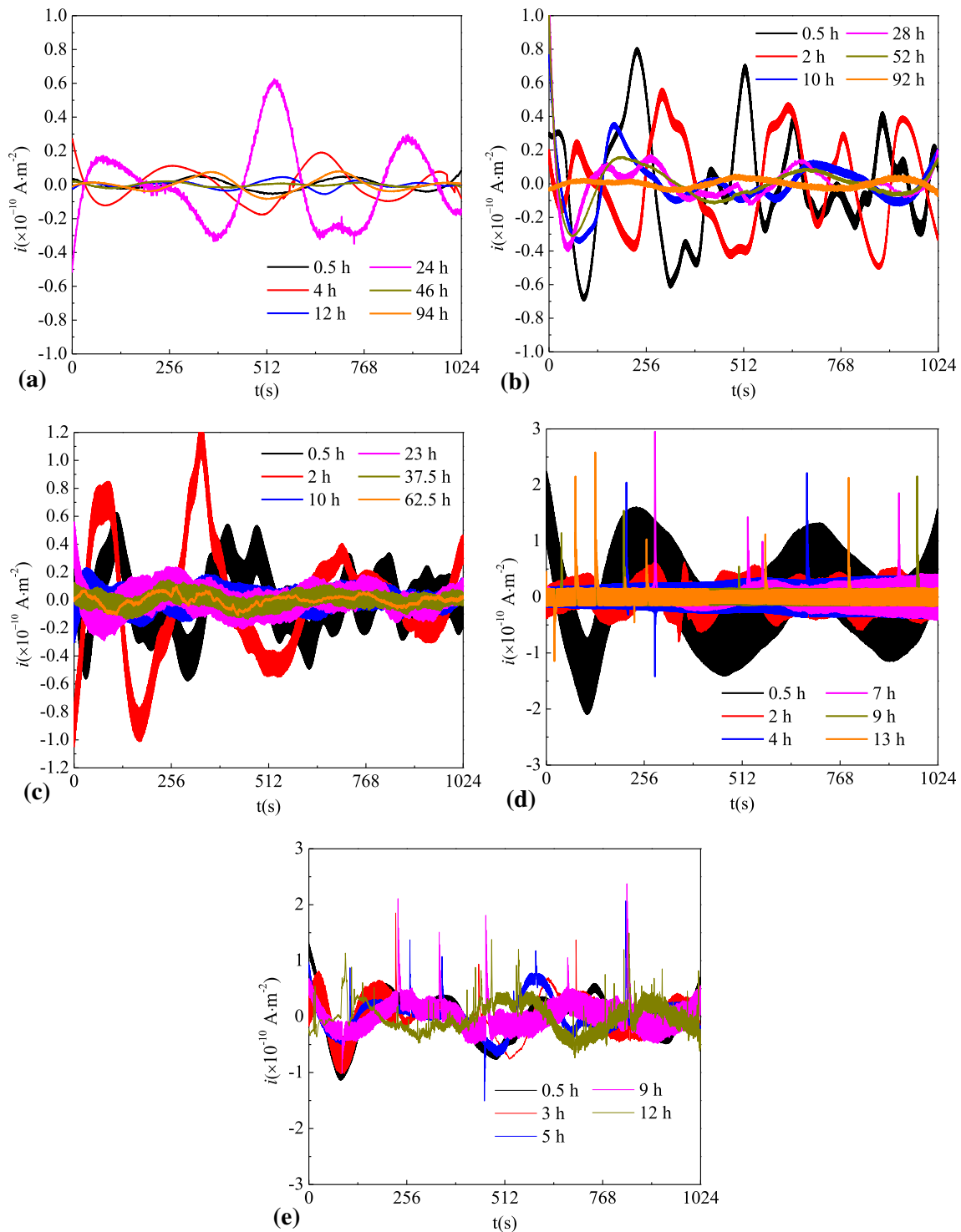
3.3 EN Under Cyclic Loading

3.3.1 Analysis in Time Domain. Figure 6 shows the time-domain current noise spectrums of E690 steel fatigued in the simulated seawater under different peak stresses. Direct current drifts are removed in all the spectrums by the polynomial fitting method. The highest order of polynomial fitting is five, and the windows size is 2048 (1024 s) (Ref 24). Figure 6(a), (b) and (c) shows that transient peaks are not found on the current noise at any immersion period when peak stress ranges from zero to 0.8 $\sigma_{p0.2}$. When the peak stress approaches to and surpasses the proof strength (Fig. 6d and e), the transient peaks appear and their occurrence rate increases evidently not only with cycling time elapsed but also with increased peak stress.

Figure 7 shows the magnified view of one current transient peak in time-domain current spectrum. It is seen that the current signal increases sharply and then decays exponentially to the base level in about ten seconds. This feature was usually found in the pitting process of low-carbon steels (Ref 25) or pure metals (Ref 26). So each transient peak should be associated with birth and death of a metastable pit. Generally, the more frequently metastable pitting occurs, the more easily pitting corrosion can arise.

In order to get more corrosion information from time-domain spectrum, the current noise was analyzed statistically. The standard deviations (S_I) of each current noise spectrum were calculated, and the corresponding noise resistances, R_n, were calculated through the following expression:

$$R_n = S_V / S_I \qquad (Eq\ 1)$$

where S_v is the standard deviation of potential noise. Values of S_I and R_n under different peak stresses are plotted versus

Fig. 6 Time-domain current noise spectrums at different fatigue times in simulated seawater under cyclic loading with different peak stresses: (a) stress free, (b) 0.6 $\sigma_{p0.2}$, (c) 0.8 $\sigma_{p0.2}$, (d) 0.95 $\sigma_{p0.2}$, (e) 1.02 $\sigma_{p0.2}$

N/N_a in Fig. 8 and 9, respectively. Enhancement of S_I often means the increasing instability of the electrode surface and occurrence of local corrosion (Ref 27). R_n is usually of a fine consistency with polarization resistance (the value of which is approximately equal to that of R_{ct} in this paper). Generally, the decreasing R_n indicates the increasing tendency to pit nucleation and growth (Ref 28).

3.3.2 Analysis in Frequency Domain. The current noises were further analyzed in frequency domain through fast Fourier transformation. Figure 10 shows the power spectrum density curves at different corrosion fatigue time under various peak stresses. Generally, there are two important characteristic parameters about corrosion in PSD curves: ① one is the low-frequency white noise (W_I), namely the height of the
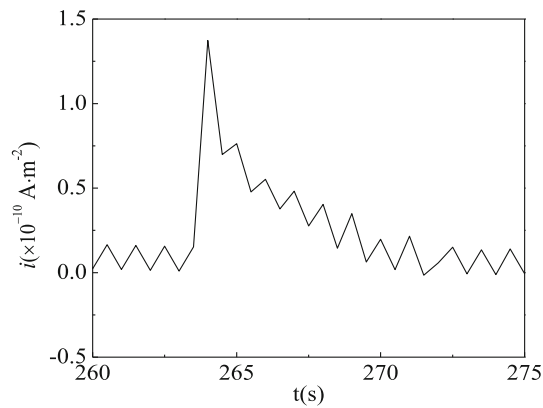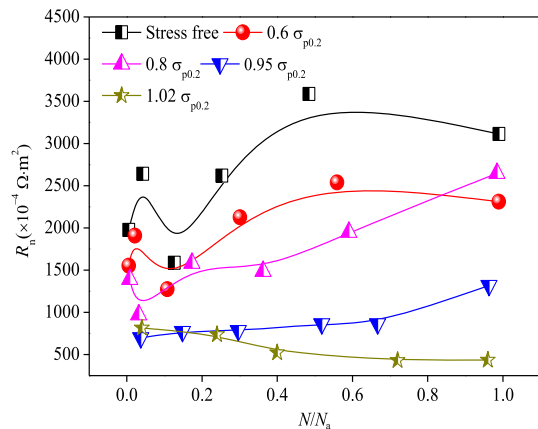
Fig. 7 Magnified view of one current transient peak in time-domain spectrum
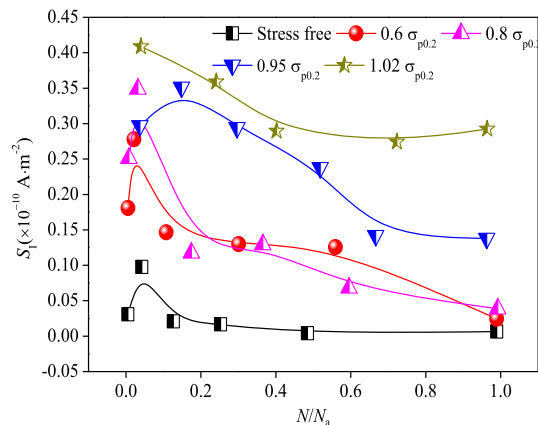
Fig. 8 Variation of the standard deviation of current noise with N/N_a under cyclic loading with various peak stresses

Fig. 9 Variation of the noise resistance with N/N_a under cyclic loading with various peak stresses

horizontal segment in the low-frequency region of PSD curves. W_I represents the base corrosion level. Generally, the greater W_I is, the faster the base corrosion rate is; ② the other one is the slope of linear segment in the middle-frequency region of PSD curves (l). The corrosion form can be figured out with its value. The greater its value is, the greater the local corrosion tendency is. The literature (Ref 29) reported that when the value was

above − 20 dB/decade, pitting corrosion would occur.

Those two parameters obtained from the PSD curves are plotted versus N/N_a in Fig. 11 and 12, respectively. Figure 11 shows that W_I increases with peak stresses increased, while it decreases with increased N/N_a. It indicates that the surface status becomes stable with increased N/N_a and unstable with elevated peak stress. The trends are consistent with the trends of S_I with N/N_a and peak stress shown in Fig. 8. Figure 12 exhibits that the value of l increases with increased peak stress and exceeds -20 dB/decade at a later stage when the peak stress is 0.95 $\sigma_{p0.2}$ and 1.02 $\sigma_{p0.2}$. Research of Uruchurtu and Dawson (Ref 30) shows that pitting corrosion is extremely likely to take place when the value of l is greater than − 20 dB/decade, while the electrode is corroded uniformly or passivated when the value of l is far lower than -20 dB/decade. Thus, it can be learned that pitting corrosion may occur on E690 steel with peak stress of 0.95 $\sigma_{p0.2}$ and 1.02 $\sigma_{p0.2}$ at the later stage.

3.4 Corrosion Morphology Under Cyclic Stress

Figure 13 shows the microscopic morphology on the side surface near the crack origin of E690 steel in simulated seawater under cyclic loading with various peak stresses. Figure 13(a) shows that stress-free E690 steel is corroded uniformly in simulated seawater. When E690 steel suffers cyclic stress, numerous secondary cracks or corrosion pits are found on the side surface near the crack origin (Fig. 13b, c, d and e). Along with increasing peak stress, more corrosion pits occur and the secondary crack size decreases. Under relatively low peak stress, the secondary crack has more time to propagate until the main crack fractures. As the peak stress is elevated, the main crack propagates faster, leaving less time for the secondary crack propagation. Moreover, the secondary cracks with smaller size would become blunt and even disappear under the attack of pitting (Ref 23). It is noted from Fig. 13(c) that the secondary cracks usually initiate from the corrosion pits. The above phenomena indicate that there may be a mechanism change along with increased peak stress. The images shown in Fig. 13 verify the results of current response and EN under cyclic loading.

4. Discussion

4.1 Effect of Cyclic Stress on the Electrochemical Process

Based on the kinetics theory of electrode process, the effects of cyclic stress on the electrochemical process of E690 steel in simulated seawater can be ascribed to three sources: ① effect of cyclic stress on the mass transfer process on the steel–seawater interface; ② effect of cyclic stress on the electric double layer; and ③ effect of cyclic stress on the surface structure. Through these three aspects, cyclic stress exerts an effect on the corrosion fatigue crack initiation.

For the first aspect, the surface status of E690 steel in simulated seawater becomes increasingly unstable with enhanced peak stress. This is reflected in Fig. 2 and 8. The up-down movement induced by cyclic stress disturbs the mass transfer of the interface. Variation of S_I with peak stress at the early fatigue stage confirms it further (Fig. 9). Along with elapsed immersion time, the concentration gradient has been established and a thin product layer forms on the electrode
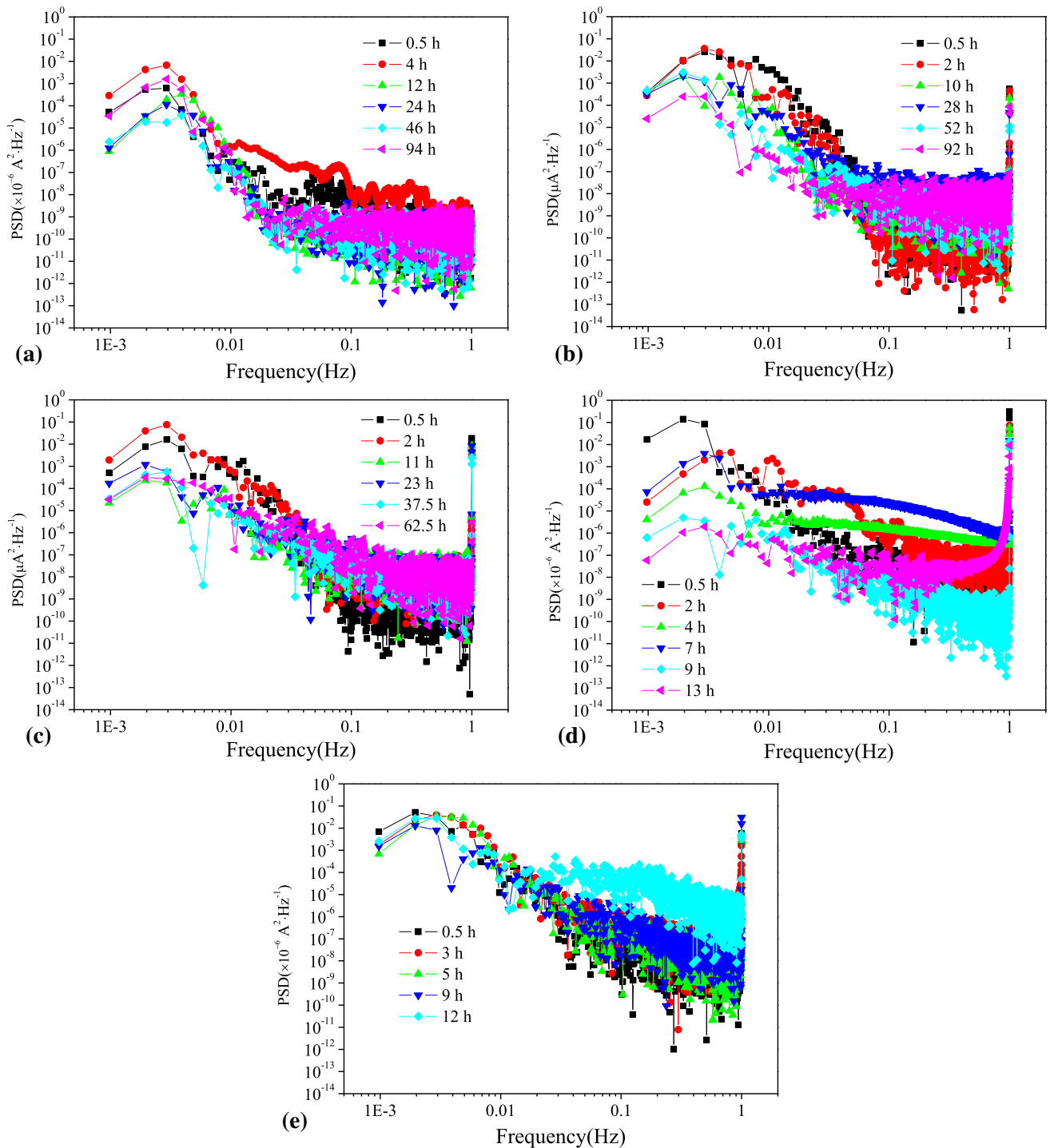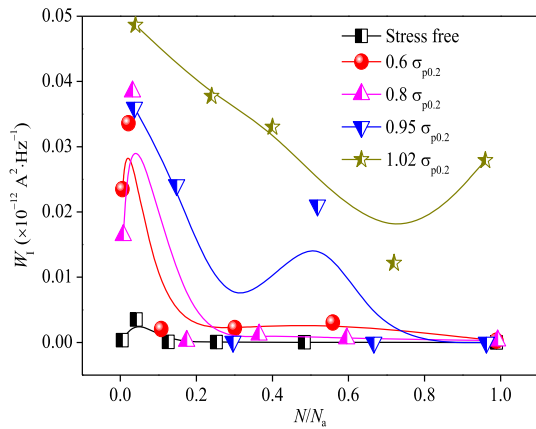
Fig. 10 Power spectrum density curves at different fatigue times under various peak stresses: (a) stress free, (b) 0.6 $\sigma_{p0.2}$, (c) 0.8 $\sigma_{p0.2}$, (d) 0.95 $\sigma_{p0.2}$, (e) 1.02 $\sigma_{p0.2}$

surface. The status of the electrode surface becomes more stable at a later fatigue stage. Thus, S_I decreases with increased N/N_a.

For the second aspect, the effects of cyclic stress on the electric double layer include two processes: the faradic process and the non-faradic process. The faradic process is mainly reflected on the variation of R_{ct} with peak stress. As shown in Fig. 3, cyclic stress has a positive effect on promoting the electrochemical reactions. It could be attributed to the

mechanochemical or chemomechanical effects (Ref 3), i.e., the higher that the stress level is, the lower that the activation energy of electrochemical reaction is. R_{ct} shows a different trend with N/N_a when peak stress is below or above the proof strength (Fig. 3). The reason may be as follows: When E690 steel suffers cyclic loading with a peak stress below the proof strength, the substrate has not been yielded yet. The interface becomes more and more stable along with elapsed fatigue time, when the product layer thickens. Thus, R_{ct} increases with

Fig. 11 Variation of the white noise level in low-frequency region with N/N_a under various peak stresses
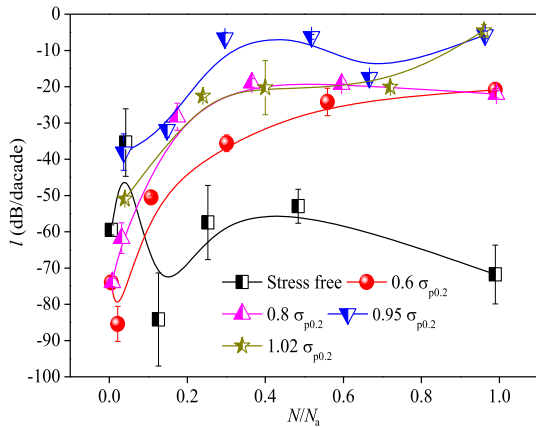
Fig. 12 Variation of the slope of the linear segment in the power spectrum density curve with N/N_a under various peak stresses

increased N/N_a when peak stress is below the proof strength. When peak stress is above the proof strength, the substrate yields, and dislocations near the surface initiate and slip outside the surface, making fresh metal constantly exposed to the seawater. As a result, R_{ct} decreases with increased N/N_a when peak stress is above the proof strength.

The non-faradic process is mainly reflected on the cyclic current response to cyclic stress, as shown in Fig. 4. Guan et al. (Ref 9) deemed that the cyclic current response was mainly caused by charging and discharging of the electric double layer and the strain-induced change in surface area and the mechanochemical effect could be negligible. Ignoring the film breakdown and the pitting process, the non-faradic current I_{nF} can be calculated as:

$$I_{nF} = A\varphi \frac{dC}{dt} + AC \frac{d\varphi}{dt} \qquad (Eq\ 2)$$

where A is the exposed area of the electrode, C is the capacitance, dC/dt is the rate of change in capacitance and $d\varphi/dt$ is the rate of change in potential. For simplification, they assumed that the potential does not change with time and concluded that the relationship between amplitude of the cyclic current response and the peak stress is linear when peak stress is below the proof strength, while it deviates greatly from linearity when the peak stress is above the proof

strength. However, they failed to realize the nature between cyclic stress and cyclic current response. Their assumption of constant potential was also baseless.

Conversely, we affirm that I_{nf} mainly results from the rate of change in potential $d\varphi/dt$. The reason is as follows: on the one hand, the change of the exposed area of the electrode, which is the main source of dC/dt, can be negligible according to Guan's calculation (Ref 9). On the other hand, the amplitude of cyclic current response under 1.02 $\sigma_{p0.2}$ barely increases compared with that under 0.95 $\sigma_{p0.2}$. Thus, it can be inferred that it is not dC/dt but $d\varphi/dt$ which makes the main contribution to I_{nf}. It is also verified by the literature (Ref 7), which revealed that cyclic stress could change the atomic energy state on the electrode surface. Furthermore, the potential of the electric double layer is closely associated with the atomic energy state on the electrode surface. Thus, it can be inferred that cyclic stress changes the potential of the electric double layer by changing the atomic energy state, consequently inducing the variation of current response. As a result, the amplitude of the current response increases with increased peak stress. And when the peak stress is above the proof strength (1.02 $\sigma_{p0.2}$), some dislocations initiate and the specimen yields, limiting the enhancement of the amplitude of current response.

For the third aspect, contact angles (θ) of distilled water were measured on E690 steel in air with various constant stresses. A contact goniometer (Dataphasics Instrument Co. Ltd, Model: OCA 20) was used to measure the contact angle. A desktop fatigue machine (CARE Measurement and Control Co. Ltd, 1.5 kN) was used to load the constant stress. The measurement details could be seen in our previous work (Ref 23). Each contact angle was the average of five-time measurements in different areas on the work section. Figure 14 shows the images of contact angle measurements under different constant stresses. Before measurement, the sample surface was ground with emery papers from 400 to 5000 grit and then electrochemically polished with 10 vol.% perchloric acid in acetic acid for 60 s. The voltage is 24.5 V. As is well known, the contact angle is closely related to the surface energy. Their relationship can be expressed by the Owens–Wendt–Kaelble–Uy theory (Ref 31), as follows.

$$\gamma_{LV}(1 + \cos\theta) = 2\sqrt{\gamma_S^d \gamma_{LV}^d} + 2\sqrt{\gamma_S^d \gamma_{LV}^d} \qquad (Eq\ 3)$$

where γ_{LV} is the liquid–gas interface energy; γ_S^d is the solid dispersion force; γ_{LV}^d is the liquid–gas dispersion force; γ_S^p is the solid polar force; and γ_{LV}^p is the liquid–gas polar force. The solid surface energy (γ_S) is the sum of γ_S^d and γ_S^p.

$$\gamma_S = \gamma_S^d + \gamma_S^p \qquad (Eq\ 4)$$

γ_S^p can be neglected for metals due to their non-polarity. And γ_{LV}, γ_{LV}^d and γ_{LV}^p are constant during the measurement. So it can be learned from Eq 3 and 4 that the smaller value of θ is, the greater value of γ_S is. Thus, it is inferred that γ_S of E690 steel increases with increasing stress level. Figure 15 shows the variation of contact angle with constant stress level. It can be seen that the contact angle decreases linearly with stress level below 0.95 $\sigma_{p0.2}$. This is consistent with Kiejna and Pogosov's research results (Ref 32). They found that there is a positive linear relationship between metal surface energy and elastic strain. It is also noted from Fig. 15 that the relationship deviates from linearity when the stress level approaches to or surpasses the proof strength. It should be attributed to the new produced
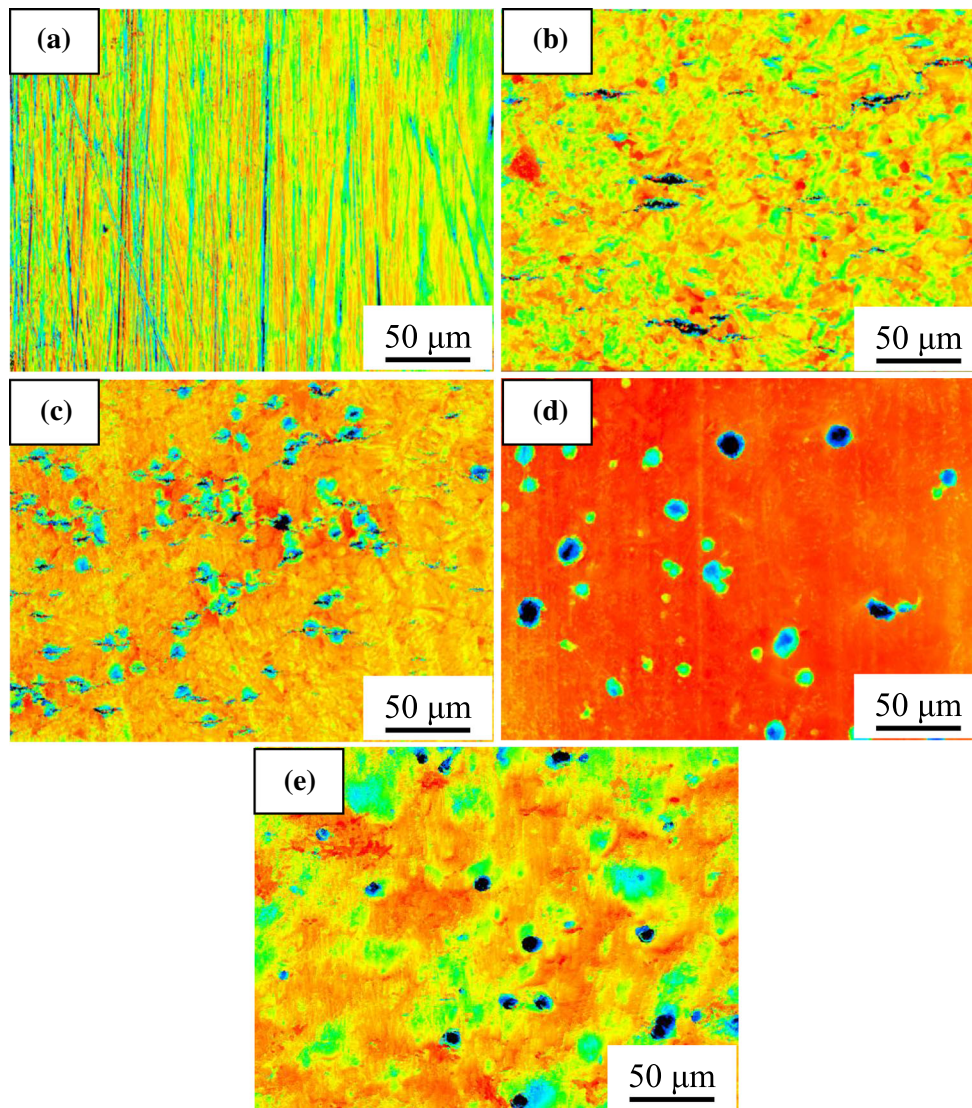
Fig. 13 Microscopic morphology on side surface near the crack origin of E690 steel in simulated seawater under cyclic loading with various peak stresses: (a) stress free, (b) 0.6 $\sigma_{p0.2}$, (c) 0.8 $\sigma_{p0.2}$, (d) 0.95 $\sigma_{p0.2}$, (e) 1.02 $\sigma_{p0.2}$
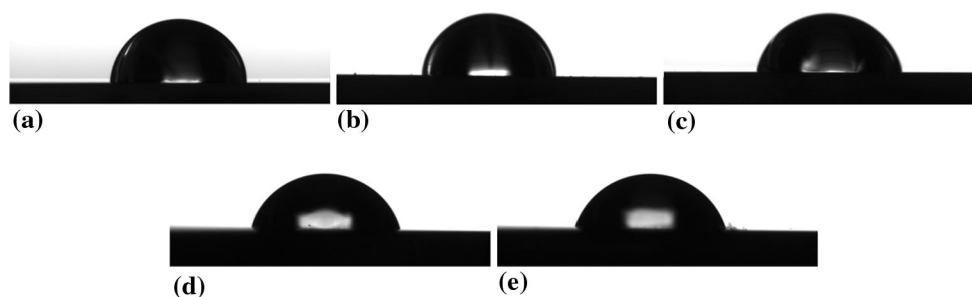
Fig. 14 Image of contact angle of distilled water with E690 steel in air under various constant stresses: (a) stress free, (b) 0.6 $\sigma_{p0.2}$, (c) 0.8 $\sigma_{p0.2}$, (d) 0.95 $\sigma_{p0.2}$, (e) 1.02 $\sigma_{p0.2}$

dislocation outcrops and slip steps induced by local deformation, which was characterized in our previous study (Ref 23) and other relevant reports (Ref 33, 34). The dislocation outcrops and slip steps greatly increase the surface energy, thus inducing the deviation from linearity. It can be learned that under cyclic stress with peak stress approaching to or above the proof strength, the dislocation outcrops and slip bands can repeatedly generate on the surface, thus promoting the localized anodic dissolution.
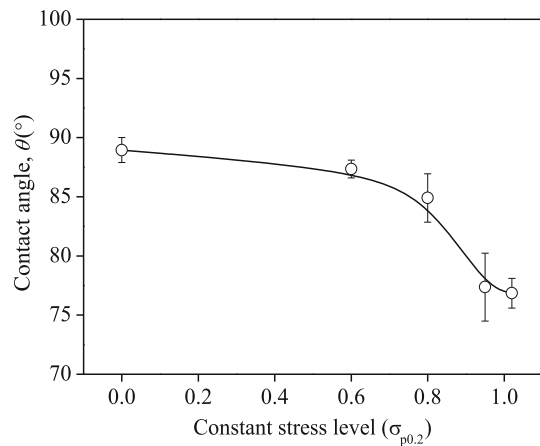
Fig. 15 Variation of contact angle of distilled water with E690 steel in air on constant stress level

4.2 Effect of Cyclic Stress on Corrosion Fatigue Crack Initiation

Due to the great influence of the surface structure on corrosion fatigue crack initiation, the above discussion about effect of cyclic stress on the surface structure of E690 steel can provide important information about its fatigue crack initiation in simulated seawater. When the peak stress is below the proof strength, cyclic stress does not change the surface structure of E690 steel. Defects on the surface, such as grain boundaries and phase boundaries, will preferentially be dissolved due to higher electrochemical activity inducing by local residual stress and atomic disorder. Then, the dissolved boundaries are cracked under stress concentration, inducing narrow and straight cracks as shown in Fig. 13(b). This crack initiation mode was also observed and described in the literature (Ref 35). Since the peak stress is relatively low, all cracks propagate slowly at the early stage. The secondary cracks can propagate for relatively long time before rapid propagation of the main crack. As a result, numerous secondary cracks are found on the side surface of E690 steel under peak stresses of 0.6 $\sigma_{p0.2}$ and 0.8 $\sigma_{p0.2}$ (Fig. 13b and c). When the peak stress approaches to or surpasses the proof strength, the formed dislocation outcrops and slip bands are dissolved to be corrosion pits. One of the largest corrosion pits is cracked and rapidly propagates to fracture under cyclic loading with higher peak stress.

The different crack initiation modes under various peak stresses are also reflected on the results of EN under cyclic loading. In time-domain analysis, current transients were observed on the time-domain spectrums under peak stress of 0.95 $\sigma_{p0.2}$ and 1.02 $\sigma_{p0.2}$ (Fig. 6d and e), while not seen on those under peak stress of 0.6 $\sigma_{p0.2}$ and 0.8 $\sigma_{p0.2}$ (Fig. 6b and c). In frequency-domain analysis, the slope of the linear segment of PSD curve is greater than -20 dB/decade under peak stress of 0.95 $\sigma_{p0.2}$ and 1.02 $\sigma_{p0.2}$ (Fig. 12). Both of them indicate that the corrosion type of E690 steel in simulated seawater transforms to pitting corrosion along with the peak stress surpassing the proof strength. Consequently, the corrosion fatigue crack initiation mode changes along with the peak stress surpassing the proof strength.

5. Conclusion

Based on the above discussions, the following conclusions can be drawn.

1. The charge transfer resistance (R_{ct}) of E690 steel in simulated seawater decreases with the peak stress of cyclic loading increasing from elastic range to above the proof strength. Continuous increasing R_{ct} with cycling time under peak stress above the proof strength indicates that continuous fresh metal induced by work-softening exposes to the seawater.
2. The charge and discharge of electric double layer, which induce the cyclic current response under cyclic stress, are mainly ascribed to the stress-induced potential change of electric double layer.
3. Corrosion type of E690 steel in simulated seawater transforms to pitting corrosion along with the peak stress approaching to and surpassing the proof strength, resulting in the mechanism of corrosion fatigue crack initiation transforming to pit-inducing cracking.

Acknowledgments

References

1. C.E. Jaske, *Corrosion Fatigue of Metals in Marine Environments*, Springer, Berlin, 1981
2. C. Laird, D.J. Duquette, Mechanisms of fatigue crack nucleation, in *Corrosion Fatigue, Chemistry, Mechanics and Microstructure*, presented at NACE, Houston, USA, 1972, p 88
3. E.M. Gutman, *Mechanochemistry of Solid Surface*, World Scientific Press, Singapore, 1994
4. R. Ebara, Corrosion Fatigue Crack Initiation in 12% Chromium Stainless Steel, *Mater. Sci. Eng. A*, 2007, **468–470**, p 109
5. W. Zhao, Y. Wang, T. Zhang, and Y. Wang, Study on the Mechanism of High-Cycle Corrosion Fatigue Crack Initiation in X80 Steel, *Corros. Sci.*, 2012, **57**, p 99
6. T. Pyle, V. Rollins, and D. Howard, The Influence of Cyclic Plastic Strain on the Transient Dissolution Behavior of 18/8 Stainless Steel in 3.7 M H_2SO_4, *J. Electrochem. Soc.*, 1974, **122**, p 1445
7. Y.F. Li, G.C. Farrington, and C. Laird, Cyclic Response-Electrochemical Interaction in Mono and Polycrystalline AISI, 316L Stainless Steel in H_2SO_4 Solution-I. The Influence of Mechanical Strain on the Transient Dissolution Behavior During Corrosion Fatigue, *Acta Mater.*, 1993, **41**, p 693
8. E. Tada, K. Noda, S. Kumai, and T. Tsuru, Monitoring of Corrosion Fatigue Cracking Using Harmonic Analysis of Current Responses Induced by Cyclic Stressing, *Corros. Sci.*, 2004, **46**, p 1549
9. L. Guan, B. Zhang, X.P. Yong, J.Q. Wang, E.H. Han, and W. Ke, Effect of Cyclic Stress on the Metastable Pitting Characteristic for 304 Stainless Steel Under Potentiostatic Polarization, *Corros. Sci.*, 2015, **93**, p 80
10. L. Guan, B. Zhang, X.P. Yong, Y. Zhou, J.Q. Wang, E.H. Han, and W. Ke, Quantitative Understanding of the Current Responses Under Elastic Cyclic Loading for 304 Stainless Steel, *J. Electrochem. Soc.*, 2016, **163**, p C627

11. C. Patel, T. Pyle, and V. Rollins, The Influence of Cyclic Plastic Deformation on Electrode Reactions on Mild Steel in Aqueous Chloride Solutions of Varying pH, *Met. Sci.*, 1977, **11**, p 185

12. J. Ma, B. Zhang, J. Wang, G. Wang, E.H. Han, and W. Ke, Anisotropic 3D Growth of Corrosion Pits Initiated at MnS Inclusions for A537 Steel During Corrosion Fatigue, *Corros. Sci.*, 2010, **52**, p 2867

13. A.R. Despic, R.G. Raicheff, and J.O.M. Bockris, Mechanism of the Acceleration of the Electrodic Dissolution of Metals During Yielding Under Stress, *J. Chem. Phys.*, 1968, **49**, p 926

14. K. Jones and D.W. Hoeppner, Pit-to-Crack Transition in Pre-corroded 7075-T6 Aluminum Alloy Under Cyclic Loading, *Corros. Sci.*, 2005, **47**, p 2185

15. S.I. Rokhlin, J.Y. Kim, H. Nagy, and B. Zoofan, Effect of Pitting Corrosion on Fatigue Crack Initiation and Fatigue Life, *Eng. Fract. Mech.*, 1999, **62**, p 425

16. Y.F. Cheng and J.L. Luo, Metastable Pitting of Carbon Steel Under Potentiostatic Control, *J. Electrochem. Soc.*, 1999, **146**, p 970

17. J. Racek, M. Stora, P. Šittner, L. Heller, J. Kopeček, and M. Petrenec, Monitoring Tensile Fatigue of Superelastic NiTi Wire in Liquids by Electrochemical Potential, *Shape Memory Superelast.*, 2015, **1**, p 204

18. H. Emi, M. Yuasa, A. Kumano, T. Arima, N. Yamamoto, and M. Umino, A Study on Life Assessment of Ships and Offshores Structures: 3rd Report: Corrosion Control and Condition Evaluation for a Long Life Service of the Ship, *J. Soc. Nav. Archit. Jpn.*, 1993, **174**, p 735

19. H. Emi, M. Yuasa, A. Kumano, H. Kumamoto, N. Yamamoto, and M. Matsunaga, A Study on Life Assessment of Ships and Offshores Structures: 2nd Report: Risk Assessment of Fatigue Failures of Hull Structures, *J. Soc. Nav. Archit. Jpn.*, 1992, **172**, p 627

20. K.J. Miller and R. Akid, The Application of Microstructural Fracture Mechanics to Various Metal Surfaces States, *Mater. Sci.*, 1997, **33**, p 1

21. M.A. Daeubler, G.W. Warren, I.M. Bernstein, and A.M. Thompson, Modeling of Corrosion Fatigue Crack Initiation Under Passive Electrochemical Conditions, *Metal. Mater. Trans. A*, 1991, **22**, p 521

22. Q. Guo, J. Liu, M. Yu, and S. Li, Effect of Passive Film on Mechanical Properties of Martensitic Stainless Steel 15-5PH in a Neutral NaCl Solution, *Appl. Surf. Sci.*, 2015, **327**, p 313

23. T. Zhao, Z. Liu, C. Du, C. Dai, X. Li, and B. Zhang, Corrosion Fatigue Crack Initiation and Initial Propagation Mechanism of E690 Steel in Simulated Seawater, *Mater. Sci. Eng. A*, 2017, **708**, p 181

24. Y. Qiu, J. Huang, and X. Guo, Trend Removal in the Analysis of Electrochemical Noise by Polynomial Fitting, *J. Huazhong Univ. Sci. Tech.*, 2005, **33**, p 39

25. Y.F. Cheng, M. Wilmott, and J.L. Luo, Analysis of the Role of Electrode Capacitance on the Initiation of Pits for A405 Carbon Steel by Electrochemical Noise Measurement, *Corros. Sci.*, 1999, **41**, p 1245

26. C.B. Breslin and A.L. Rudd, Activation of Pure Al in an Indium-Containing Eletrolyte—an Electrochemical Noise and Impedance Study, *Corros. Sci.*, 2000, **42**, p 1023

27. Z. Jia, C. Du, and X. Li, Detection of Pitting Corrosion of 316L Stainless Steel in FeCl$_3$ Solution by Electrochemical Noise, *Corros. Prot.*, 2011, **32**, p 497

28. F. Mansfeld and H. Xiao, Electrochemical Noise Analysis of Iron Exposed to NaCl Solutions of Different Corrosivity, *J. Electrochem. Soc.*, 1993, **140**, p 2205

29. C.C. Lee and F. Mansfeld, Analysis of Electrochemical Noise Data for a Passive System in the Frequency Domain, *Corros. Sci.*, 1998, **40**, p 959

30. J.C. Uruchurtu and J.L. Dawson, Noise Analysis of Pure Aluminum Under Different Pitting Conditions, *Corrosion*, 1987, **43**, p 19

31. D.K. Owens and R. Wendt, Estimation of the Surface Free Energy of Polymers, *J. Appl. Polym. Sci.*, 1969, **13**, p 1741

32. A. Kiejna and V. Pogosov, Simple Theory of Elastically Deformed Metals: Surface Energy, Stress, and Work Function, *Phys. Rev. B*, 2000, **62**, p 10445

33. H.C. Wu, B. Yang, S.L. Wang, and M.X. Zhang, Effect of Oxidation Behavior on the Corrosion Fatigue Crack Initiation and Propagation of 316LN Austenitic Stainless Steel in High Temperature Water, *Mater. Sci. Eng. A*, 2015, **633**, p 176

34. Z. Cui, Z. Liu, L. Wang, X. Li, C. Du, and X. Wang, Effect of Plastic Deformation on the Electrochemical and Stress Corrosion Cracking Behavior of X70 Steel in Near-Neutral pH Environment, *Mater. Sci. Eng. A*, 2016, **677**, p 259

35. S. Xu, X.Q. Wu, E.H. Han, W. Ke, and Y. Katada, Crack Initiation Mechanisms for Low Cycle Fatigue of Type 316Ti Stainless Steel in High Temperature Water, *Mater. Sci. Eng. A*, 2008, **490**, p 16